Journal of Computational Physics **171,** 534–559 (2001)
doi:10.1006/jcph.2001.6792, available online at http://www.idealibrary.com on IDEAL®

A Dual-Reciprocity Boundary Element Method for Evaluating Bulk Convective Transport of Surfactant in Free-Surface Flows

Samir N. Ghadiali,* David Halpern,† and Donald P. Gaver III*

*Department of Biomedical Engineering, Tulane University, New Orleans, Louisiana 70118; and †Department of Mathematics, University of Alabama, Tuscaloosa, Alabama 35487
E-mail: donald.gaver@tulane.edu

Received May 15, 2000; revised March 26, 2001

We present a dual-reciprocity boundary element method (DRBEM) to investigate bulk surfactant transport dynamics in a free-surface flow system under steady-state conditions. This free-surface flow system consists of semi-infinite bubble progression in a rigid axisymmetric capillary tube. Once adsorbed to the air–liquid interface with a surface concentration Γ, surfactant alters the interfacial surface tension γ. As the interfacial stress balance, which governs the fluid mechanics, is a function of γ, a strong coupling exists between surfactant transport dynamics and the fluid mechanics (physicochemical hydrodynamics). To model this problem over a range of bulk concentrations, C, the bulk convective/diffusive transport of surfactant to the interface must be calculated. In this paper, DRBEM is used to simulate the bulk convection–diffusion relationship while the boundary element method (BEM) is used to solve Stokes flow, and a finite-difference method is used to solve the surface transport equation under steady-state conditions. A nonlinear Langmuir adsorption model is used to determine the surfactant equation of state $\gamma = f(\Gamma)$. The validity of the DRBEM is first demonstrated by comparing computational and analytical solutions for a test problem. Next, the computational algorithm is used to calculate the bulk concentration field surrounding the bubble as a function of the far-downstream quantity of surfactant, C_o, and its influence on interfacial dynamics. These profiles clearly demonstrate the importance of accurately calculating the bulk concentration field under moderate C_o conditions. In addition, the variation of mechanical properties of this system as a function of C_o indicates that the interfacial pressure jump can be significantly larger when the bulk transport of surfactant to the interface is limited.

Key Words: dual-reciprocity boundary element method; boundary element method; Langmuir kinetics; Langmuir equation of state; pulmonary surfactant; multiphase flow; interfacial mechanics; axisymmetric; interfacial stress balance; physicochemical hydrodynamics.

0021-9991/01 $35.00

1. INTRODUCTION

The goal of this paper is to describe methods for computing bulk-phase convection–diffusion transport dynamics of surface-active substances (surfactants) in multiphase free-surface flows. Transport in these systems can be very complex because of interactions between the surfactant and the mechanical properties of the system (physicochemical hydrodynamics). As an example, we consider the mechanics of bubble progression in a fluid-filled capillary tube which is of interest in several industrial and clinical environments. This system has been used to model two-phase flow through porous media and therefore has industrial applications related to foam mobility control and enhanced oil recovery. The flow of bubbles or drops in a capillary tube also has clinical relevance since this system can be used to model the flow of blood cells through capillaries [22] as well as the embolic events that occur when air bubbles appear in the microcirculation during surgery. In addition, the progression of a finger of air in a flexible or rigid tube has been used to model the reopening of collapsed or obstructed pulmonary airways [7, 31].

The original theoretical investigation of semi-infinite bubble progression was performed by Bretherton [4] and Park and Homsy [19] using lubrication theory. However, the lubrication analysis of this system is only valid at very small capillary number, $Ca < 10^{-2}$, where $Ca = \mu U/\gamma$, μ is the fluid viscosity, U is the bubble velocity, and γ is the surface tension. Several investigators have used a variety of computational techniques to obtain results at larger *Ca* under constant surface tension conditions. Reinelt and Saffman [25] used a finite-difference formulation in conjunction with a multigrid scheme to obtain results at $10^{-2} < Ca < 2$. Other investigators [9, 27] have used the finite element method (FEM) to obtain results at $10^{-4} < Ca < 10^{1}$. Martinez and Udell [15, 16] obtained similar results using the more efficient and accurate boundary element method (BEM). Halpern and Gaver [11] presented a boundary element solution for the time-dependent motion of a semi-infinite bubble in a two-dimensional channel. Their study, which could simulate very large range of *Ca* ($10^{-1} \leq Ca \leq 10^{4}$), used a mixed boundary condition technique to improve the accuracy of the standard BEM formulation.

In addition to these surfactant-free studies, several investigators [10, 24, 28] have studied the interaction between surfactant physicochemistry and fluid mechanics in a semi-infinite bubble progression model. Ratulowski and Chang [24] found that the presence of trace quantities of surfactants could increase the dimensionless reopening pressures under diffusion-limited conditions. Stebe and Barthès-Biesel [28] used lubrication theory to demonstrate that an increase in the dimensionless pressure could also occur at elevated surfactant concentrations if adsorption processes were slow. A limitation of these models is the assumption of static equilibrium in the bubble cap region. Specifically, the surface tension in the bubble cap region was assumed to be uniform and equal to the equilibrium value, γ_{eq}. Thus, these studies do not capture the O(1) deviations from equilibrium that may arise in this system.

The most common technique to compute nonequilibrium surfactant interactions in a free-surface system is a combined BEM and finite difference scheme. Specifically, BEM is capable of modeling Stokes flow conditions, while the finite difference scheme can be used to solve the surface transport equations. Several investigators have used this technique to study the effect of insoluble surfactants on the surface of closed bubbles and drops. For an insoluble surfactant, the bulk concentration is not important since surfactant molecules reside only on the interface. Stone and Leal [29] investigated the deformation and breakup of liquid drops, while Milliken *et al.* [17] and Eggleton *et. al.* [6] studied the stretching of

a viscous drop under uniaxial extensional flow conditions. Recently, Johnson and Borhan [12] used the boundary integral technique to study the effects of surfactant on the motion and deformation of finite liquid drops in Poiseuille flow through circular tubes. Yap and Gaver [31] used this technique to investigate the importance of surfactant physicochemistry in flexible-walled systems intended to emulate collapsible airways. They predicted that surfactant uptake could significantly influence the mechanics of airway reopening.

Note that none of these hybrid BEM-finite difference techniques can simulate the bulk-phase convection–diffusion transport dynamics of surfactant. However, experiments have demonstrated that the bulk transport of pulmonary surfactants can significantly influence the physicochemical hydrodynamic behavior of the system [8]. Therefore, in the present study, we seek to develop methods that are capable of simulating bulk surfactant transport dynamics under conditions that are far from equilibrium. To do so, we have implemented a technique known as the dual-reciprocity boundary element method (DRBEM) to simulate surfactant bulk transport dynamics [20]. This DRBEM scheme couples with the BEM and finite difference schemes, which have been shown to accurately compute the surfactant physicochemical hydrodynamics in these free-surface flows.

2. DUAL-RECIPROCITY BOUNDARY ELEMENT METHOD

To accomplish the goal of investigating bulk transport dynamics in free-surface flows, we first need to develop techniques for simulating convective–diffusive transport. Solving the bulk convection–diffusion equation in a free-surface geometry using standard finite-element or finite-difference techniques is complicated because of the irregular internal mesh structure that might exist. Instead, we implement the dual-reciprocity boundary element method (DRBEM) [20] which can efficiently simulate the steady-state convection–diffusion equation. As will be demonstrated below, this method is grid-free (but still uses internal nodes), and can be efficiently implemented in a manner similar to the boundary element method. Below, we present the details of this method, and validate this approach by solving a model test problem and comparing analytical and computational results. Then, in the remainder of this paper, we implement this algorithm to solve the bulk transport of surfactant during the physiologically significant problem of bubble progression in a rigid capillary tube as a demonstration of the usefulness of this technique in free-surface flows.

2.1. *Method Implementation*

Under steady-state conditions, the bulk concentration field, $C(z, r)$, will be governed by the dimensionless convection–diffusion equation

$$\nabla^2 C = Pe(\boldsymbol{u} \cdot \nabla)C, \tag{2.1}$$

where $Pe = UR/D_{mol}$ is the Peclet number relating convection to diffusion in the system, D_{mol} is the bulk diffusion coefficient, U is a velocity scale, and R is a length scale (see Section 3 for details).

We define the right-hand side of (2.1) as the function $b(z, r)$, represented with the following approximation

$$b(z, r) = Pe(\boldsymbol{u} \cdot \nabla)C = \sum_{j=i}^{N+L} \phi_j(z, r)\alpha_j. \tag{2.2}$$

Here N is the number of boundary nodes, and L is the number of internal nodes, ϕ_j represents $N + L$ radial based interpolating functions [23] (see Appendix for details), and α_j are the unknown coefficients that will be used to satisfy (2.1).

To transform (2.1) to a boundary integral equation, we specify that each ϕ_j must satisfy

$$\phi_j = \nabla^2 f_j. \tag{2.3}$$

In the Appendix we present the axisymmetric forms of ϕ_j and f_j (as well as the appropriate derivatives) which are derived from their 3-D counterparts as detailed by Sarler [26]. Once f_j is known, a solution of (2.1) is found by using a weighted residual technique and applying Green's theorem [20] to create the boundary integral equation,

$$c_k C(\boldsymbol{x}) = \int_S K(\boldsymbol{x},\boldsymbol{y}) q \, dS_y - \int_S Q(\boldsymbol{x},\boldsymbol{y}) C \, dS_y + \sum_{j=1}^{N+L} \alpha_j \left[c_k f_j + \int_S Q(\boldsymbol{x},\boldsymbol{y}) f_j \, dS_y - \int_S K(\boldsymbol{x},\boldsymbol{y}) f_j' \, dS_y \right]. \tag{2.4}$$

Here K and Q are concentration and concentration gradient kernels given in [3] and c_k are coefficients which depend on whether the point $\boldsymbol{x}$ lies in the interior ($c_k = 1$) or on a smooth boundary ($c_k = 1/2$). The normal component of the concentration gradient at the boundary is represented by $q = dC/d\hat{\boldsymbol{n}}$, and $f_j' = df_j/d\hat{\boldsymbol{n}}$. Note that f_j must be calculated at L interior points as well as N boundary points. Equation (2.4) is integrated over a collocation vector, $\boldsymbol{y}$, that defines the boundary, S_y. The solution vector, C, is a function of a load vector, $\boldsymbol{x}$, which is defined by both internal and boundary nodes.

The DRBEM procedure involves discretizing the boundary into N_{elm} three-point quadratic elements to obtain the discretized version of (2.4),

$$\sum_{m=1}^{N_{elm}} \int_{S_m} Q(\boldsymbol{x},\boldsymbol{y}) C \, dS_m - \sum_{m=1}^{N_{elm}} \int_{S_m} K(\boldsymbol{x},\boldsymbol{y}) q \, dS_m = \sum_{j=1}^{N+L} \alpha_j \left[c_k f_j + \sum_{m=1}^{N_{elm}} \int_{S_m} Q(\boldsymbol{x},\boldsymbol{y}) f_j \, dS_m - \sum_{m=1}^{N_{elm}} \int_{S_m} K(\boldsymbol{x},\boldsymbol{y}) f_j' \, dS_m \right], \tag{2.5}$$

where N_{elm} is the number of boundary elements. Performing these integrations along each element results in the following system of linear equations,

$$\boldsymbol{Q}C - \boldsymbol{K}q = (\boldsymbol{Q}\boldsymbol{F} - \boldsymbol{K}\boldsymbol{F}')\alpha. \tag{2.6}$$

Here, $\boldsymbol{Q}$ and $\boldsymbol{K}$ are, respectively, $N \times N + L$ and $N \times 3N/2$ matrices, C is an $N + L$ vector of boundary and internal nodal concentrations, q is a $3N/2$ vector of boundary concentration gradients normal to the surface, $\boldsymbol{F}$ is an $N + L \times N + L$ matrix of f_j values, $\boldsymbol{F}'$ is a $3N/2 \times N + L$ matrix of f_j' values, and α is an $N + L$ vector of unknown coefficients. Note that $\boldsymbol{F}$ is formed by $N + L$ evaluations of f_j at each of the $N + L$ boundary and internal points, while $\boldsymbol{F}'$ is formed by $N + L$ evaluations of f_j' at $3N/2$ boundary points. We have allowed for $3N/2$ values of f_j' and q at the N boundary points to account for

discontinuities of the normal vector that can exist at the intersection between two elements that define the corners of the domain.

In order to satisfy Eq. (2.1), we complete the DRBEM formulation by expressing α in terms of the nodal concentration values. So, from (2.2),

$$\alpha = \phi^{-1} b = Pe\phi^{-1}\left(u_r \frac{\partial C}{\partial r} + u_z \frac{\partial C}{\partial z}\right), \tag{2.7}$$

where u_r and u_z are respectively the radial and axial fluid velocities in an axisymmetric coordinate system, and ϕ is an $N+L \times N+L$ matrix formed by $N+L$ evaluations of ϕ_j at each of the $N+L$ boundary and internal points. The concentration C is approximated using the same ϕ_j functions used in (2.2). So,

$$C = \phi\zeta, \tag{2.8}$$

where C is an $N+L$ vector of nodal concentrations and ζ is an $N+L$ vector of unknown coefficients. By differentiating (2.8) and using the inverse relationship, $\zeta = \phi^{-1}C$, (2.7) becomes,

$$\alpha = \left[Pe\,\phi^{-1}\left(u_r \frac{\partial \phi}{\partial r}\phi^{-1} + u_z \frac{\partial \phi}{\partial z}\phi^{-1}\right)\right] C = [\boldsymbol{R}]C, \tag{2.9}$$

where $\boldsymbol{R}$ is an $N+L \times N+L$ matrix. From this expression, (2.6) becomes

$$(\boldsymbol{Q} - \boldsymbol{S})C = \boldsymbol{K}q, \tag{2.10}$$

where $\boldsymbol{S} = (\boldsymbol{QF} - \boldsymbol{KF})[\boldsymbol{R}]$ is an $N \times N+L$ matrix.

The boundary conditions can now be used to rearrange (2.10) into $\boldsymbol{A}v = d$, where $\boldsymbol{A}$ is an $N+L \times N+L$ matrix, v is an $N+L$ vector containing unknown boundary values (concentration and concentration gradients) as well as the unknown internal concentration values, and d is an $N+L$ vector containing the known boundary value information. Therefore, all boundary and internal values can be determined by solving this system of linear equations.

In summary, DRBEM requires boundary conditions, either concentration, concentration gradient, or a linear combination, at each node along the boundary. The use of an interpolating function that satisfies (2.3) yields a surface integral solution to the bulk transport equation. However, these interpolating functions are dependent on the location of internal nodes. Therefore, the unknown internal concentrations must be determined in conjunction with boundary values. Note that DRBEM does not require that the internal nodes be placed in a structured fashion, although it is important to place the nodes in positions of large concentration gradients. Since the boundary changes shape during free-surface problems, the unstructured nature of the internal nodes eliminates the costly re-meshing step required by other techniques (finite-element and finite-difference methods). As a result, the DRBEM algorithm can efficiently determine the bulk concentrations within the interior as well as along the boundary.

2.2. *Method Validation*

To assess the validity of the DRBEM technique, we solve a model problem and compare the computational and analytical solutions. The test problem is defined by the axisymmetric

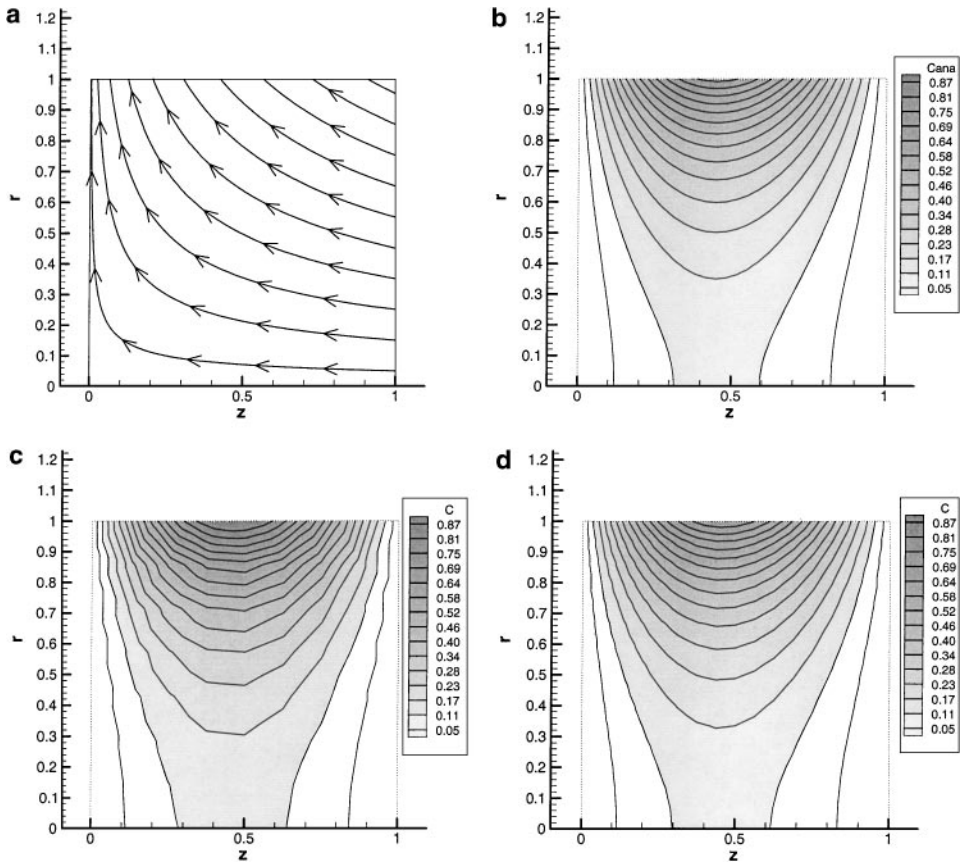

FIG. 1. (a) Domain and flow field used to test the accuracy of DRBEM. Concentration profiles for the (b) analytical solution (c) DRBEM solution with 49 internal nodes and (d) DRBEM solution with 225 internal nodes.

domain shown in Fig. 1a with a stagnation flow field ($u_z = -2z, u_r = r$). Since this flow field contains nonzero axial and radial velocities, this problem can be used to test the accuracy of both the radial and axial terms in (2.7) and (2.9). We solve (2.1) with $Pe = 1$ using the following boundary conditions,

$$\begin{aligned} \frac{dC}{dr} &= 0 \quad \text{at } r = 0; \\ C &= 0 \quad \text{at } z = 0 \quad \text{and} \quad z = 1; \\ \frac{dC}{dr} &= 10z\,{}_1F_1\left(\frac{1}{2} + \frac{\lambda_e^2}{4}; \frac{3}{2}; -z^2\right) \quad \text{at } r = 1. \end{aligned} \tag{2.11}$$

Here ${}_1F_1$ is the confluent hypergeometric function defined by Abramowitz and Stegun [1], and the eigenvalue, $\lambda_e = 3.339$, is chosen such that $dC/dr = 0$ at $z = 1$. These boundary conditions are chosen such that (2.1) has the following analytical solution for $Pe = 1$,

$$C(r, z) = \frac{20_z}{\lambda_e^2\,{}_1F_1\left(1 + \frac{\lambda_e^2}{2}; 2; \frac{1}{2}\right)}\,{}_1F_1\left(\frac{\lambda_e^2}{2}; 1; \frac{r^2}{2}\right){}_1F_1\left(\frac{1}{2} + \frac{\lambda_e^2}{4}; \frac{3}{2}; -z^2\right), \tag{2.12}$$

for comparison to the computational prediction.

TABLE I
Average Relative Error as a Function of the Number of Interior, L, and Boundary Nodes, N, for the Test Problem

Number of Interior Nodes L	Average Relative Error $C_{err}^{avg} = \frac{1}{L}\sum_{i=1}^{L} \frac{\lvert C_i - C_{ana_i}\rvert}{C_{ana,i}} \times 100\%$	
	N = 31	N = 91
25	9.21%	1.75%
49	4.83%	0.990%
100	2.90%	0.516%
225	2.10%	0.239%
784	1.38%	0.0722%

Figure 1b demonstrates this analytical solution while Figs. 1c and 1d demonstrate the DRBEM solution using 49 and 225 internal points, respectively. The solution with 225 internal nodes demonstrates that the DRBEM is able to accurately predict the analytical concentration values. As shown in Table I, the average relative error between the computational and analytical solution decreases as the number of internal points, L, increases. This decrease in error is due to the fact that a large number of internal nodes will more accurately approximate the concentration gradients that determine the body force terms b in (2.2). Table I also demonstrates that the solution accuracy will be a function of the number of boundary nodes, N. Specifically, the accuracy of the integrations in (2.5) depends on the number of boundary elements, N_{elm}, which is a direct function of N. Therefore, at small $N(=31)$ the accuracy of the boundary integrations limits the accuracy of the solution and thus the average relative error does not approach zero at large L. However, at large $N(=91)$, where boundary integrations are more accurate, the average relative error does approach zero at large L. We will now demonstrate the use of the DRBEM for simulating the bulk-transport of surfactant during a model free-surface flow problem.

3. FREE-SURFACE PROBLEM FORMULATION

In the remainder of this paper we investigate a theoretical model of semi-infinite bubble progression in a rigid axisymmetric capillary tube with a radius R (Fig. 2). The displaced

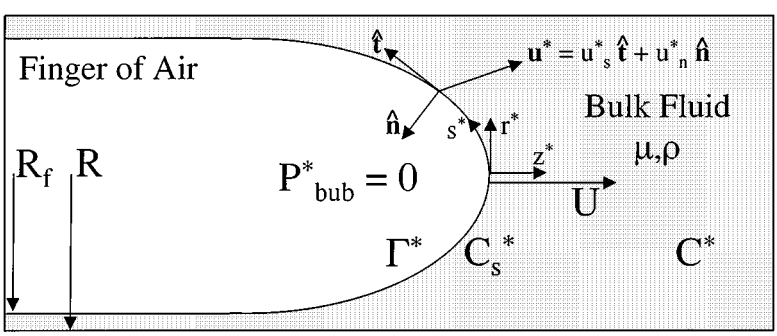

FIG. 2. Schematic representation of the theoretical model in an axisymmetric coordinate system.

fluid, which can contain surfactant, has a viscosity μ and density ρ. We consider the steady-state movement of this bubble with a forward velocity U. The air–liquid interface is defined at each point by a unit normal, $\hat{\boldsymbol{n}} = (n_z, n_r)$, a unit tangent, $\hat{\boldsymbol{t}} = (t_z, t_r)$, and a fluid velocity, $\boldsymbol{u}^* = (u_z^*, u_r^*)$, vector. The gas phase viscosity is assumed to be negligible, the finger width in the thin film region is R_f, and the constant air pressure inside the bubble is used as the reference pressure ($P_{bub}^* = 0$). Surfactant molecules can exist either in the bulk solution with concentration C^*, at the subsurface with concentration C_s^*, or adsorbed onto the interface with concentration Γ^*. The shape of the air–liquid interface $r^*(s^*)$ and $z^*(s^*)$, the local surface tension $\gamma^*(s^*)$, the surface concentration $\Gamma^*(s^*)$, and the subsurface concentration $C_s^*(s^*)$ are functions of the arc-length variable s^*.

3.1. *Governing Equations*

We use the following scaling arguments to obtain dimensionless governing equations.

$$\begin{gathered} s^* = Rs, \quad r^* = Rr, \quad z^* = Rz, \quad \boldsymbol{u}^* = U\boldsymbol{u} \\ C^* = C_o C, \quad \gamma^* = \gamma_{eq}\gamma, \quad \Gamma^* = \Gamma_\infty \Gamma, \quad P^* = \frac{\gamma_{eq}}{R}\Pi. \end{gathered} \tag{3.1}$$

Here starred ("*") variables indicate dimensional quantities, and the associated unstarred variables are dimensionless. The term C_o is the far-field bulk concentration, γ_{eq} is the equilibrium surface tension, Γ_∞ known as the maximum monolayer packing value is the surface concentration when all adsorption sites are filled, and Π is the dimensionless fluid pressure.

Hydrodynamics. With these scales, the dimensionless Navier–Stokes and continuity equations are

$$Ca\,Re\left(\frac{\partial \boldsymbol{u}}{\partial t} + (\boldsymbol{u}\cdot\nabla)\boldsymbol{u}\right) + \nabla\Pi = Ca\nabla^2\boldsymbol{u} \quad \text{and} \quad \nabla\cdot\boldsymbol{u} = 0. \tag{3.2}$$

Here, $Re = \rho U R/\mu$ is the Reynolds number which relates inertial to viscous forces, and $Ca = \mu U/\gamma_{eq}$ is the Capillary number which relates viscous to surface tension forces. When inertial forces are negligible ($Re^*Ca \ll 1$), Eq. (3.2) reduces to the steady-state Stokes equations,

$$\nabla\Pi = Ca\nabla^2\boldsymbol{u} \quad \text{and} \quad \nabla\cdot\boldsymbol{u} = 0, \tag{3.3}$$

which demonstrates that viscous stresses are balanced by the fluid pressure gradient. To complete the hydrodynamic description, we must impose boundary conditions on the domain shown in Fig. 3. At steady-state these conditions are

$$\frac{\partial u_z}{\partial r} = 0, \quad u_r = 0 \quad \text{at} \quad r = 0 \quad \text{for } z > 0 \tag{3.4}$$

$$\boldsymbol{u}\cdot\hat{\boldsymbol{n}} = u_z n_z + u_r n_r = 0 \quad \text{at } r = r_m(z) \tag{3.5}$$

$$\sigma_{fluid}\cdot\hat{\boldsymbol{n}} = \gamma\kappa\hat{\boldsymbol{n}} + \frac{d\gamma}{ds}\hat{\boldsymbol{t}} \quad \text{at } r = r_m(z) \tag{3.6}$$

$$\boldsymbol{u} = n_z \quad \text{as} \quad z \to -\infty \tag{3.7}$$

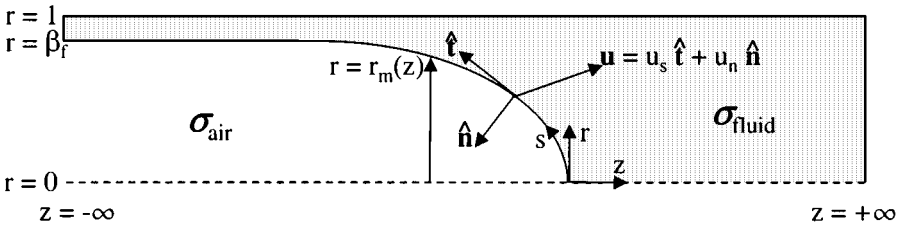

FIG. 3. Schematic of the fluid boundary and the location of the imposed boundary conditions.

$$u_r = 0, \quad u_z = -1 \quad \text{at } r = 1 \tag{3.8}$$

$$\boldsymbol{u} = \left[2\beta_f^2(r^2 - 1)\right] n_z \quad \text{as } z \to +\infty. \tag{3.9}$$

Here, $\beta_f = R_f/R$ is the dimensionless width of the air bubble in the thin film. Equation (3.4) mandates symmetry at the centerline. The kinematic boundary conditions (3.5), (3.7), (3.8), and (3.9) are stated in terms of the bubble-fixed reference frame at steady-state. Equation (3.5) specifies no penetration at the interface while (3.8) specifies no-slip at the tube wall. Equation (3.7) imposes a plug flow boundary condition far upstream in the static thin film while (3.9) imposes a parabolic Poiseuille flow far downstream which satisfies a global conservation of mass relationship. Finally, Eq. (3.6) represents the interfacial stress-balance where $\sigma_{fluid} = -\Pi \boldsymbol{I} + Ca(\nabla \boldsymbol{u} + \nabla^T \boldsymbol{u})$ represents the fluid stress tensor ($\sigma_{air} = 0$ since $\mu_{air} \approx 0$ and $P^*_{bub} = 0$). Since the interface is a free-surface (i.e., its position and shape are not known *a priori*), boundary conditions are supplied for the velocity as well as the stress at the interface (3.5) and (3.6). As explained further in Section 3.3, one boundary condition (the stress balance) will be imposed and the interface shape will be iterated until the other boundary condition (no penetration) is satisfied.

Interfacial Transport and Mechanics. Under steady-state conditions where $\boldsymbol{u} \cdot \hat{\boldsymbol{n}} = 0$, the dimensionless surface transport equation,

$$\begin{gathered} \nabla_s \cdot (\Gamma u_s) = Pe_s^{-1} \nabla_s^2 \Gamma + j_n \\ \text{where: } j_n = \frac{St_a}{\lambda} C_s (1 - \Gamma) - St_d \Gamma, \end{gathered} \tag{3.10}$$

will govern the distribution of adsorbed surfactant molecules. Here, ∇_s is a surface gradient operator, u_s is the surface velocity, $Pe_s = UR/D_{int}$ is the surface Péclet number which relates surface convection rates to surface diffusion rates, and D_{int} is the surface diffusion coefficient. The mass flux of surfactant to the interface, j_n, is governed by the adsorption Stanton number, $St_a = k_a \Gamma_\infty / U$, where k_a is the adsorption rate coefficient, the desorption Stanton number, $St_d = k_d R/U$, where k_d is the desorption rate coefficient, and the dimensionless adsorption depth, $\lambda = \Gamma_\infty/(C_o R)$, where C_o is the far downstream bulk concentration. The adsorption Stanton number, St_a, relates adsorption rates to surface convection rates, St_d relates desorption rates to surface convection rates, while λ is related to the fluid thickness that contains sufficient surfactant molecules to bring the interfacial concentration to Γ_∞. Note that $St_\lambda = St_a/\lambda$ is the effective adsorption parameter which relates adsorption rates to interfacial creation rates. Equation (3.10) states that the rate of change in Γ as a result of surface convection is balanced by a surface diffusive flux and the mass flux of surfactant to the interface.

The following boundary conditions complete the surface transport problem

$$\frac{\partial \Gamma}{\partial s} = 0 \quad \text{at} \quad s = 0 \tag{3.11}$$

$$\frac{\partial \Gamma}{\partial s} = 0 \quad \text{as} \quad s \to \infty. \tag{3.12}$$

These Neumann boundary conditions specify symmetry at the centerline (3.11) and no variation in the static thin film (3.12).

The mass flux term, j_n, in (3.10) is based on a Langmuir model in which a certain number of adsorption sites are available. The surface concentration when all sites are filled is known as the maximal monolayer packing concentration (Γ_∞). Thus, the adsorption term, $(St_a/\lambda)C_s(1-\Gamma)$, is proportional to the subsurface concentration as well as the number of free sites while the desorption term, $St_d\Gamma$, is proportional to the number of filled sites. Solving $j_n = 0$ yields,

$$\Gamma = \frac{\Gamma^*}{\Gamma_\infty} = \frac{St_\lambda C_s}{St_\lambda C_s + St_d}. \tag{3.13}$$

In order to determine the relationship between surface tension and surface concentration (the surfactant equation of state) the thermodynamic Gibb's relationship [18],

$$d\gamma = -El\ \Gamma d(\ln C_s) \tag{3.14}$$

can be used with (3.13) to obtain the nonlinear Langmuir equation of state

$$\gamma(\Gamma) = 1 + El \ln \frac{1-\Gamma}{1-\tilde{\Gamma}_{eq}} \tag{3.15}$$

Here, $El = \mathbb{R}T\Gamma_\infty/\gamma_{eq}$ is the elasticity number which is a measure of a surfactant's ability to modify the interfacial surface tension; $\mathbb{R}$ is the universal gas constant; T is the temperature; and $\tilde{\Gamma}_{eq} = \Gamma_{eq}/\Gamma_\infty$ is the dimensionless equilibrium surface concentration, where Γ_{eq} is the concentration that is in equilibrium with the far-downstream bulk concentration, C_o. Note that Γ_{eq} can be determined from (3.13) by setting $C_s = 1$

$$\tilde{\Gamma}_{eq} = \frac{St_\lambda}{St_\lambda + St_d}. \tag{3.16}$$

Although other investigators [24] have identified the measure of a surfactant's strength with the Marangoni number, *Ma*, we follow the more traditional definition [28] such that *Ma* is related to the ratio of Marangoni to viscous stresses, i.e., $Ma = El/Ca = \mathbb{R}T\Gamma_\infty/\mu U$.

Bulk Transport. The governing equation for steady-state convection and diffusion of surfactant in the bulk solution is given by

$$(\boldsymbol{u}\cdot\nabla)C = Pe^{-1}\nabla^2 C. \tag{3.17}$$

Here $Pe = UR/D_{mol}$ is the bulk Péclet number which relates convection rates to diffusion rates, and D_{mol} is the bulk diffusion coefficient. The following boundary conditions complete the bulk transport formulation:

$$\frac{\partial C}{\partial r} = 0 \quad \text{at } r = 0 \tag{3.18}$$

$$\frac{1}{Pe\lambda}(\hat{\boldsymbol{n}}\cdot\nabla)C = St_\lambda C_s(1-\Gamma) - St_d\Gamma \quad \text{at } r = r_m(z) \tag{3.19}$$

$$\frac{\partial C}{\partial z} = 0 \quad \text{as } z \to -\infty \tag{3.20}$$

$$\frac{\partial C}{\partial r} = 0 \quad \text{at } r = 1 \tag{3.21}$$

$$C = 1 \quad \text{as } z \to +\infty. \tag{3.22}$$

These boundary conditions specify symmetry at the centerline (3.18), no axial variation in the static thin film (3.20), no surfactant flux into the tube wall (3.21), and a constant far-downstream bulk concentration (3.22). The interfacial boundary condition (3.19) specifies continuity between the bulk diffusive flux and adsorptive/desorptive fluxes at the interface.

3.2. *Computational Methods*

Hydrodynamics. The boundary element method (BEM) is used to solve the hydrodynamic aspects of this problem. Ladyzhenskaya [13] showed that a solution of (3.3) could be obtained by using Fourier transforms and applying Green's theorem,

$$u_k(\boldsymbol{x}) = \int_S T_{ik}(\boldsymbol{x},\boldsymbol{y})u_i\,dS - \frac{1}{Ca}\int_S U_{ik}(\boldsymbol{x},\boldsymbol{y})\tau_i\,dS, \tag{3.23}$$

where T_{ik} and U_{ik} are known as traction/velocity kernels, u_i is the velocity vector, and $\tau_i = \sigma_{fluid}\cdot\hat{\boldsymbol{n}}$ is the traction vector. The axisymmetric form of U_{ik} and T_{ik} have been reported in Becker [3]. As $\boldsymbol{x}$ approaches a point on the boundary, (3.23) can be rewritten in discretized form as

$$c_{ki}u_i(x) - \sum_{m=1}^{N_{elm}}\int_{S_m} T_{ik}(\boldsymbol{x},\boldsymbol{y})u_i\,dS_m = \frac{1}{Ca}\sum_{m=1}^{N_{elm}}\int_{S_m} U_{ik}(\boldsymbol{x},\boldsymbol{y})\tau_i\,dS_m, \tag{3.24}$$

where c_{ki} accounts for the stress discontinuities at that occur at the surface, the boundary is discretized into N_{elm} three-point quadratic elements, and S_m indicates the boundary of an element. The integrands in (3.24), which are integrated over each element, can be calculated using regular and logarithmic Gaussian quadrature techniques [11]. Upon integration (3.24) can be expressed as

$$\boldsymbol{T}w = \boldsymbol{U}t. \tag{3.25}$$

Here $\boldsymbol{T}$ and $\boldsymbol{U}$ are, respectively, $2N \times 2N$ and $2N \times 3N$ matrices, and $w_{2j-1} = u_{zj}$, $w_{2j} = u_{rj}$, $t_{2j-1} = \tau_{zj}$, $t_{2j} = \tau_{rj}$, where $j = 1, 2, \ldots, N$ represents the number of boundary nodes. Matrix $\boldsymbol{U}$ is made larger than $\boldsymbol{T}$ to allow the stress vector to have two distinct values at corner points where the normal vector can be discontinuous. This feature is useful during the implementation of mixed boundary conditions at corner points (see Section 3.3). In a well-posed problem, either the velocities or the stresses are known at each node point. These boundary conditions are used to rearrange (3.25) into a system of linear equations of the form $\boldsymbol{A}v = d$, where $\boldsymbol{A}$ is a $2N \times 2N$ matrix, v is a $2N$ vector containing the unknown velocities and stresses, and d is a $2N$ vector containing the known stress or velocity information. This system is solved for the unknown velocities and stresses, v, using Gaussian elimination.

Finally, once all boundary values are known, (3.23) can be used to calculate velocities at any point inside the domain (which will be necessary for transport calculations).

Surfactant Transport. The bulk concentration field, $C(r, z)$, is calculated using the DRBEM algorithm described in detail in Section 2. Note that the subsurface concentration, C_s, is defined by the bulk concentration, C, at the air–liquid interface. The term C_s is used in the surface-transport calculations below.

In order to solve the surface-transport (3.10) for $\Gamma(s)$ we implement a one-dimensional finite difference scheme. For axisymmetric problems, Stone [29] demonstrated that (3.10) can be rewritten as

$$\begin{aligned}\frac{1}{r}\frac{\partial}{\partial s}(\Gamma u_s r) &= \frac{1}{Pe_s}\frac{1}{r}\frac{\partial}{\partial s}\left(r\frac{\partial \Gamma}{\partial s}\right) + St_\lambda C_s(1-\Gamma) - St_d\Gamma \quad \text{for } r > 0\\ 2\frac{\partial}{\partial s}(\Gamma u_s) &= \frac{2}{Pe_{int}}\frac{\partial^2\Gamma}{\partial s^2} + St_\lambda C_s(1-\Gamma) - St_d\Gamma \quad \text{at } r = 0,\end{aligned} \tag{3.26}$$

where the equation at $r = 0$ is obtained by taking the appropriate limits. In order to efficiently solve (3.26), we implemented a five-point unequally spaced central differencing scheme for the derivatives of Γ[2]. This method provides the surface concentrations at all interfacial node points.

3.3. *Implementation Considerations*

Interfacial Geometry. The computational solution will require an accurate representation of the interfacial geometry. Specifically, the interfacial stress balance boundary condition at the free interface (3.6) requires an accurate calculation of the local interfacial curvature, κ. In addition, the BEM and DRBEM techniques depend on an accurate calculation of the normal vector, $\hat{\boldsymbol{n}}$, at the interface. Finally, the FDM method requires an accurate calculation of the interfacial arc-length variable, s.

To provide these geometric properties accurately, the arc-length at each node point, s_i, is determined by integrating along the interface using a piecewise cubic polynomial approximation to the interface shape. As a result, the discrete functional relationship between the axial and radial position of each node and the arc-length, i.e., $z(s_i)$ and $r(s_i)$, are known. Cubic splines are then computed for z_i vs s_i and r_i vs s_i with specified end derivative conditions to ensure symmetry. These splines are then differentiated to compute the normal and tangential vectors,

$$n_z = -\frac{dr}{ds}, \quad n_r = \frac{dz}{ds}, \quad t_z = n_r, \quad t_r = -n_z, \tag{3.27}$$

and the interfacial curvature,

$$\begin{aligned}\kappa &= \frac{dr}{ds}\frac{d^2z}{ds^2} - \frac{dz}{ds}\frac{d^2r}{ds^2} + \frac{1}{r}\frac{dz}{ds} \quad \text{for } r > 0\\ \kappa &= 2\left(\frac{dr}{ds}\frac{d^2z}{ds^2} - \frac{dz}{ds}\frac{d^2r}{ds^2}\right) \quad \text{at } r = 0,\end{aligned} \tag{3.28}$$

where the equation at $r = 0$ is obtained by taking the appropriate limit as $r \to 0$.

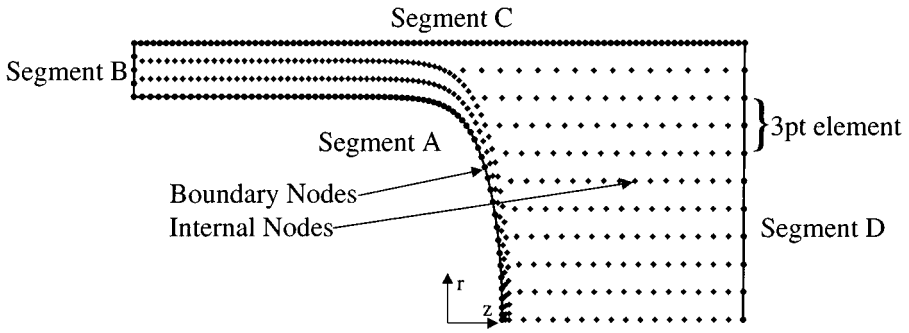

FIG. 4. Typical node distribution and computational domain size (not to scale) with segments on which the boundary conditions are applied. (●) boundary nodes, (◆) internal nodes.

Computational Domain. We use the computational domain shown in Fig. 4. Segment A represents the air–liquid interface, segment B models the thin film conditions, segment C identifies the rigid capillary wall, and segment D represents the far-downstream conditions. The nodes along these segments are the boundary nodes (●) which are used in the BEM and DRBEM calculations. Note that the symmetry axis does not have to be modeled as a boundary in the axisymmetric BEM and DRBEM techniques. Along each surface, three adjacent boundary nodes are used to construct an isoparametric quadratic element over which the BEM and DRBEM integrations are performed. Since we have implemented an unequally spaced finite-differencing technique to solve (3.26), the nodes that define the interface in the BEM and DRBEM domain can be used directly in the finite-difference calculations. Thus, the need for interpolating surface quantities (u_s, C_s) between two different grids is eliminated. The distribution of internal nodes (◆) shown in Fig. 4 is used in the DRBEM method. These nodes are placed so as to define a high internal node density near the interface where concentration gradients are expected to be large because of adsorption of surfactant from the bulk. Table II presents the typical number of nodes used for each boundary segment as well as the number of internal nodes used in this study.

Table III specifies the hydrodynamic and bulk transport variables that are applied to each segment in Fig. 4 to satisfy the boundary conditions discussed in Section 3.1. Recall that τ is the stress vector, $\tau_r = \sigma_{fluid} \cdot \boldsymbol{n}_r$, $\tau_z = \sigma_{fluid} \cdot \boldsymbol{n}_z$. The application of BEM and DRBEM with these boundary conditions would ideally produce the unknown boundary and internal values. However, as demonstrated by Halpern and Gaver [11], the discontinuity of the normal vector at corner points results in a stress vector discontinuity which can lead to erratic results. That paper demonstrated that the use of "mixed" boundary conditions at the corner points could greatly improve the solution accuracy. Therefore, we have implemented similar "mixed" boundary conditions in the current model as demonstrated in Table IV. For

TABLE II
Typical Number of Nodes Used in the Computational Domain

Segment	A	B	C	D	Internal
# of Nodes	71	5	97	11	290

TABLE III
Boundary Conditions Applied to the Computational Domain

Solver/Problem	Segment A	Segment B	Segment C	Segment D
BEM/Hydrodynamics	τ_r, τ_z (3.6)	u_r, u_z (3.7)	u_r, u_z (3.8)	u_r, u_z (3.9)
DRBEM/Bulk Transport	$dC/d\hat{\boldsymbol{n}}$(3.19)	$dC/d\hat{\boldsymbol{n}}$(3.20)	$dC/d\hat{\boldsymbol{n}}$(3.21)	C (3.22)

example, at the corner node B-C, the radial stress and axial velocity (τ_r, u_z) are applied along segment B. However, for the same node, the radial velocity and axial stress (τ_r, τ_z) are applied along segment C. Thus, the unknown quantity at this node is the axial stress for segment B and the radial stress for segment C. In order to obtain a high degree of accuracy, we have implemented these "mixed" type boundary conditions when possible.

Iteration Technique. Under steady-state conditions, two separate interfacial boundary conditions must be satisfied, the interfacial stress-balance (3.6) and the kinematic condition (3.5). Therefore, one must specify one condition and iterate the interfacial shape until the other condition is satisfied. We choose to specify the stress-balance and iterate the domain shape until the kinematic condition is satisfied. Our process involves using a Newton's method to satisfy the kinematic condition by moving node points in a direction normal to the interface shape. This is a standard method that is followed, for example, in [7, 31]. This type of iteration process is described in detail in [5].

In the process of satisfying the interfacial stress and kinematic conditions, the surfactant transport is modified because of domain modification and the subsequent modification of the flow field. This subsequently can affect the stress-balance via the equation of state (3.15), which leads to further iterations to simultaneously satisfy the transport problem. Figure 5 is a schematic representation of the steps used to solve this coupled problem and to satisfy the convergence criteria specified below. Initially, we assume an interfacial shape and surfactant distribution $\Gamma(s)$. Note that any specification or determination of $\Gamma(s)$ also results in a surface tension distribution $\gamma(s)$ via the equation of state (3.15). In step 1, the BEM is used to solve (3.3) for the bulk and interfacial velocities, $\boldsymbol{u}(z, r)$, $\boldsymbol{u}_s(s)$, given $\gamma(s)$ and the interfacial shape. In step 2, these velocities are used to solve (3.17) with the DRBEM for the bulk surfactant concentration field, $C(z, r)$. Note that the solution of (3.17) is dependent on $\Gamma(s)$ via the boundary condition in (3.19). In step 3, the new bulk surfactant distribution, $C_s(s)$, as well as the velocity field, $u_s(s)$, are used to solve (3.10) with the FDM for $\Gamma(s)$. Note that (3.10) is dependent on the subsurface concentration, $C_s(s)$. Therefore, even for a fixed velocity field, the bulk transport and surface transport are coupled. We found that

TABLE IV
Mixed Boundary Conditions Applied at Corner Nodes of the Computational Domain

	Node A-B		Node B-C		Node C-D	
Solver/Problem	Segment A	Segment B	Segment B	Segment C	Segment C	Segment D
BEM/Hydrodynamic	τ_r, τ_z	τ_r, u_z	τ_r, u_z	u_r, τ_z	u_r, τ_z	τ_r, u_z
DRBEM/Bulk Transport	$dC/d\hat{\boldsymbol{n}}$	$dC/d\hat{\boldsymbol{n}}$	$dC/d\hat{\boldsymbol{n}}$	C	C	$dC/d\hat{\boldsymbol{n}}$

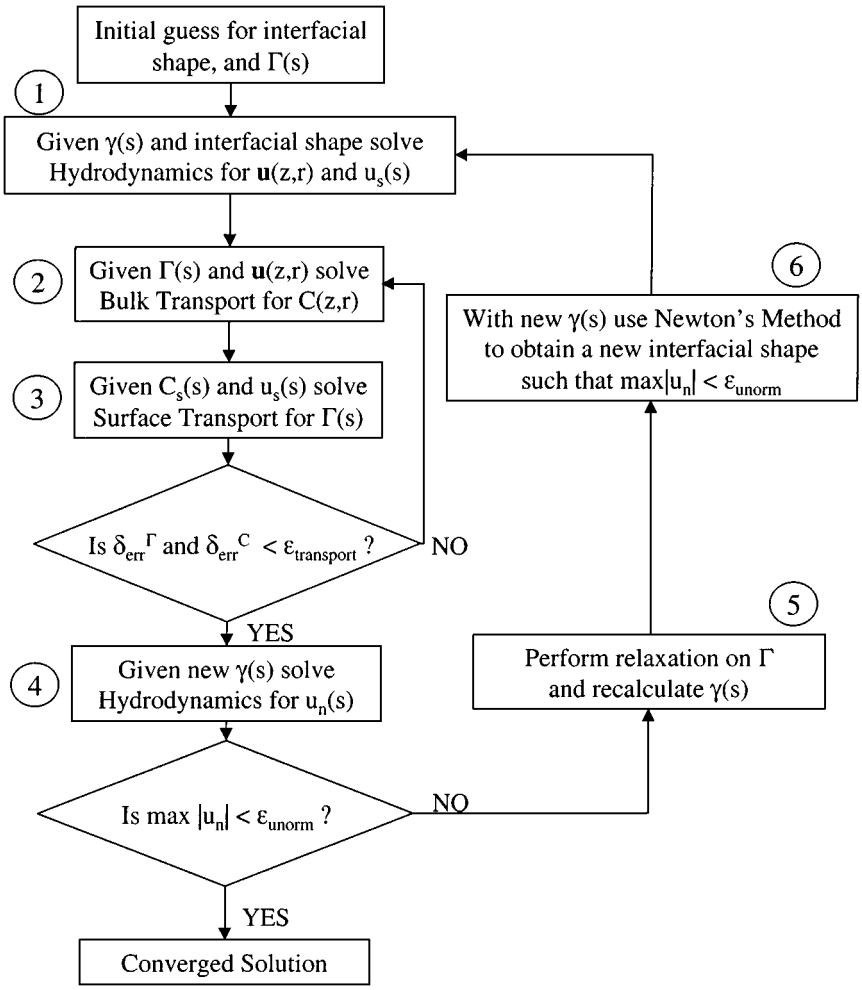

FIG. 5. Flow chart of the iterations steps used to obtain a converged solution. Note that $\gamma(s)$ can be obtain from $\Gamma(s)$ and the equation of state.

a simple fixed-point iteration scheme between C_s and Γ without relaxation was sufficient to obtain a converged solution. Convergence was determined when the sum of the relative errors between successive iterations, defined as

$$\delta_{err}^{C} = \sum_{i=1}^{N} \frac{\left|C_{s,i}^{k} - C_{s,i}^{k+1}\right|}{C_{s,i}^{k+1}}, \quad \delta_{err}^{\Gamma} = \sum_{i=1}^{N} \frac{\left|\Gamma_{i}^{k} - \Gamma_{i}^{k+1}\right|}{\Gamma_{i}^{k+1}}, \tag{3.29}$$

where k is the iteration number, are less than $\epsilon_{transport} = 10^{-4}$. In step 4, the converged concentration profiles, which determine the new $\gamma(s)$, are used to solve (3.3) for the normal velocity distribution along the interface, $\boldsymbol{u} \cdot \hat{\boldsymbol{n}} = u_n(s)$. If the maximum normal velocity is less than ϵ_{unorm}, we have satisfied the boundary condition stated in (3.5) and accept the converged solution. Note that the value for ϵ_{unorm} is based on the convergence test performed in Section 4.1. However, if this convergence criteria is not satisfied, a new interface shape must be calculated. Since changes in the stress balance at the interface, via changes in

$\gamma(s)$, can produce a highly nonlinear mechanical response, we found it useful to perform a relaxation procedure on Γ (and thus γ) before we attempted to calculate this new interfacial shape. This relaxation procedure is performed at each node point such that

$$\Gamma_i^{new} = \Gamma_i^{old} + x_d\left(\Gamma_i^{current} - \Gamma_i^{old}\right). \tag{3.30}$$

Here Γ^{old} is the concentration used in step 1, $\Gamma^{current}$ is the concentration used in step 4, Γ^{new} is the concentration to be used in the next iteration, and x_d is the damping factor. Thus, $x_d = 1$ corresponds to no relaxation in that $\Gamma^{current}$ would be used as Γ^{new}.

With the new $\gamma(s)$ we performed a Newton's method iteration [21], step 6, to obtain a new interfacial shape such that $\max|u_n| \leq \epsilon_{unorm}$. Specifically, a system of nonlinear equations is generated by relating the normal velocity at each node to the position of all interfacial nodes. By finding the roots to this system of nonlinear equations, we can adjust the interfacial shape until $\max|u_n| \leq \epsilon_{unorm}$. With this new interfacial shape, the iteration procedure is repeated until a converged solution is obtained.

4. RESULTS

4.1. *Convergence*

Recall that in the BEM solution of the hydrodynamic problem, the interfacial stress balance is explicitly satisfied since it is used as the boundary condition at the interface. However, for steady-state problems, the interfacial kinematic condition (3.5) must also be satisfied. This kinematic boundary condition is satisfied when $\max|u_n| \leq \epsilon_{unorm}$. In order to determine an appropriate value for ϵ_{unorm}, we implemented the iteration scheme with various values of ϵ_{unorm} for the base parameter case; $Ca = 0.15$, $El = 0.5$, $Pe = 10$, $Pe_s = 10^3$, $\lambda = 0.1$, $St_a = 1$, $St_d = 5$. These parameter values are chosen such that the bulk and adsorptive/desorptive transport processes are both O(1), thus demonstrating the model's ability to simulate these interrelated mechanisms. The result of these simulations, shown in Fig. 6, indicate that all system variables approach a limiting value for $\epsilon_{unorm} \leq 10^{-4}$ (dotted line in Fig. 6). Therefore, a solution is considered "converged," when the following convergence criteria are simultaneously satisfied: $\max|\boldsymbol{u}\cdot\hat{\boldsymbol{n}}| \leq 10^{-4}$, $\delta_{err}^{C} \leq 10^{-4}$, and $\delta_{err}^{\Gamma} \leq 10^{-4}$.

4.2. *Accuracy*

The accuracy of the bulk surfactant transport solution will depend on two computational variables, the domain size and the number of internal nodes. The thin-film boundary conditions for the bulk and surface transport problems (3.20) and (3.12) are defined at an infinite axial distance from the bubble tip. Therefore, if the computational domain in the thin film is truncated prematurely, the application of these thin film boundary conditions along segment B in Fig. 4 will result in an inaccurate solution. In addition, the DRBEM technique is known to present numerical problems when large concentration gradients exist in the bulk fluid which, for example, would occur if convection dominates diffusion (large *Pe*). Under these conditions, the DRBEM solution will not be accurate if the number of internal nodes is not sufficient to capture these large gradients. As shown below, the bulk concentration in the thin film can be determined analytically based on the dimensionless parameter values.

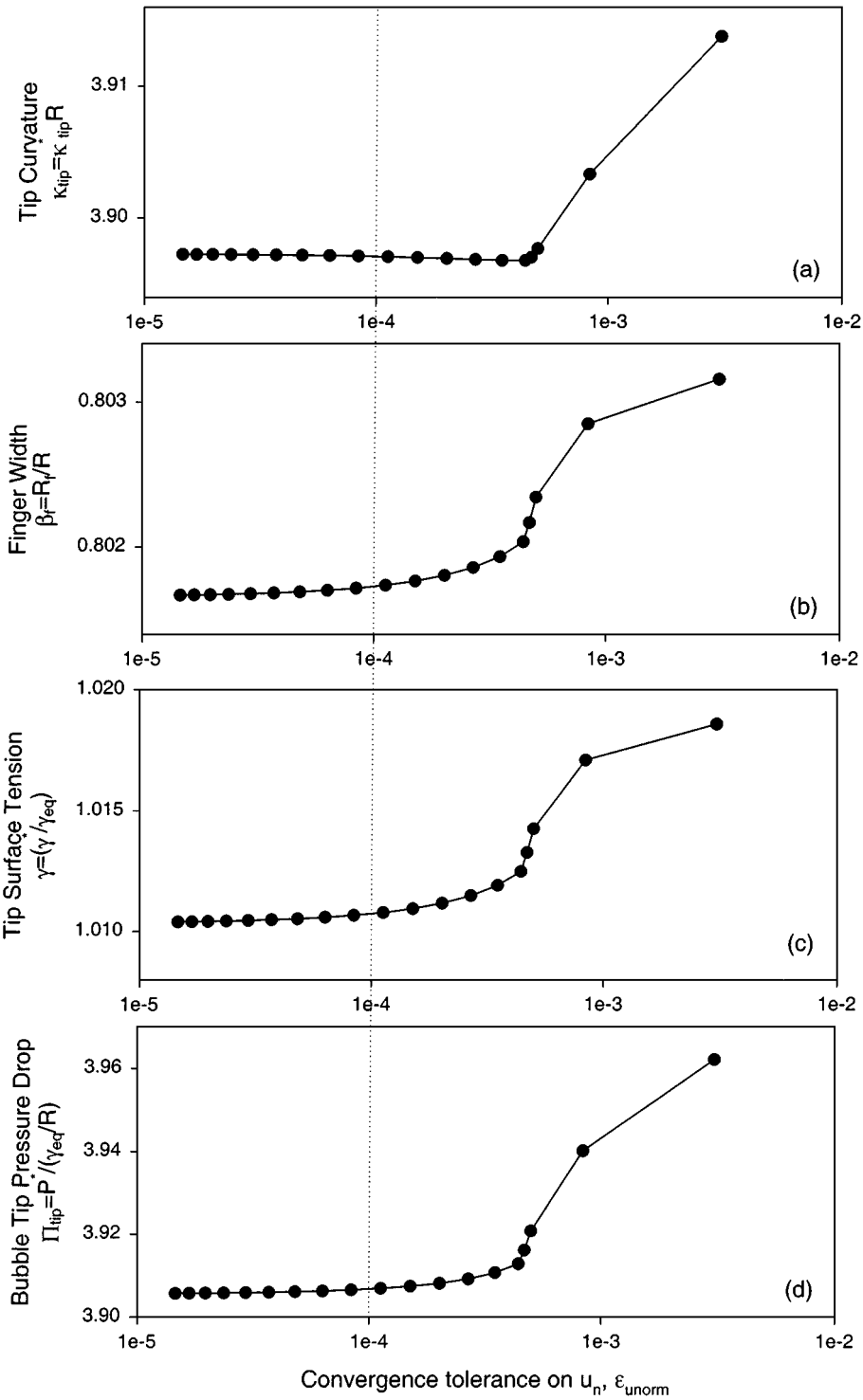

FIG. 6. Convergence profiles for (a) tip curvature (b) finger width (c) tip surface tension and (d) tip bubble pressure drop as a function of the maximum normal velocity convergence parameter, ϵ_{unorm}. Dotted line indicates the value of ϵ_{unorm} used in this study. ($Ca = 0.15$, $El = 0.5$, $Pe = 10$, $Pe_s = 10^3$, $\lambda = 0.1$, $St_a = 1$, $St_d = 5$).

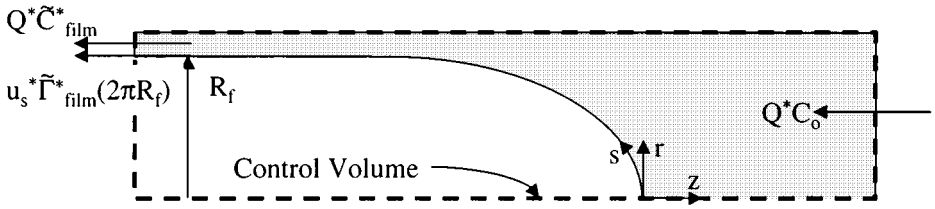

FIG. 7. Schematic diagram of the control volume and the surfactant mass fluxes used to derive the analytic value of $\tilde{C}_{film.}$

Therefore, we assess the transport solution accuracy by comparing the computational value, C_{film}, with the analytical result, $\tilde{C}_{film}$.

Far upstream in the static thin film ($z \to -\infty$), C and Γ should be in equilibrium as stated in (3.13),

$$\tilde{\Gamma}_{film} = \frac{St_\lambda \tilde{C}_{film}}{St_\lambda \tilde{C}_{film} + St_d}. \tag{4.1}$$

Here, $\tilde{\Gamma}_{film}$ and $\tilde{C}_{film}$ are used to denote the constant values in the thin film. In addition, consider the control volume in Fig. 7, which extends far enough upstream and downstream that the diffusive flux is negligible at the ends. In the bubble-tip frame of reference, surfactant enters from the downstream end and exits through the upstream end by convection in the bulk and along the interface. In dimensional terms, the overall mass balance is

$$Q^* C_o = Q^* \tilde{C}^*_{film} + u^*_s \tilde{\Gamma}^*_{film} 2\pi R_f. \tag{4.2}$$

Defining the flow rate, $Q^* = U\pi(R^2 - R_f^2)$ and using (4.2) in dimensionless form yields,

$$\tilde{\Gamma}_{film} = \frac{(1 - \tilde{C}_{film})(1 - \beta_f^2)}{2\lambda\beta_f}. \tag{4.3}$$

Equations (4.1) and (4.3) are solved simultaneously to provide the analytic value of the thin film bulk concentration, $\tilde{C}_{film}$.

In our simulations, we calculate the relative error between $\tilde{C}_{film}$ and C_{film}. If this error is less than 1%, we conclude that the domain size and number of internal nodes are sufficient to produce an accurate solution. For the base parameter case, we found that a domain size of $-6.9 < z < 4.5$ with 290 internal nodes gave a relative error of 0.07%. In all calculations, the solution accuracy according to this mass balance analysis was checked and the domain was extended in the negative z direction and/or more internal nodes were used to satisfy the condition that the relative error <1%.

4.3. *Concentration Profiles*

In the remainder of this paper we demonstrate how the computational algorithm can predict the bulk concentration field surrounding the bubble as a function of the far-downstream quantity of surfactant, C_o. Recall that the dimensionless adsorption depth $\lambda = \Gamma_\infty/(C_o R)$ is a direct function of C_o such that at low concentrations $\lambda \to \infty$ and for very high concentrations $\lambda \to 0$. In these investigations, we choose not to study the adsorption rate modifications that would be accompanied by changes in C_o. However, variations in λ would result

in variations in the effective adsorption parameter $St_\lambda = St_a/\lambda$ and therefore variations in the equilibrium point, $\tilde{\Gamma}_{eq}$, via (3.16). Also, the strength of the surfactant depends on El and $\tilde{\Gamma}_{eq}$ via (3.15). So, to maintain a fixed surfactant strength and thereby isolate the effect of changing C_o, we hold St_λ and $\tilde{\Gamma}_{eq}$ constant while λ is varied. To accomplish this, every variation in λ was accompanied by a modification of St_a such that $St_a = \lambda St_d \tilde{\Gamma}_{eq}/(1 - \tilde{\Gamma}_{eq})$. Under these conditions, the variations in λ provides a fixed effective adsorption rate (St_λ) and a fixed equilibrium point $\left(\tilde{\Gamma}_{eq}\right)$. Note that the variations in λ and St_a are performed about the base parameter values presented in Section 4.1.

Figure 8 demonstrates the bulk concentration field surrounding the semi-infinite bubble for $\lambda = 1.03\text{e-}3, 0.1, 9.07$ at a fixed $\tilde{\Gamma}_{eq}$. At very large C_o (low λ) the bulk transport processes are rapid such that the bulk concentration is uniform and nearly equal to the far-downstream value ($C = 1$). Under these conditions, the system can be considered to be in bulk-equilibrium. This bulk-equilibrium situation has been analyzed by previous investigators [28, 31]. However, at low C_o (large λ), the bulk transport of surfactant to the interface is limited. As a result, very large concentration gradients develop in the bulk fluid at high λ values. In this case, the quantity of surfactant that can be transported to the interface by bulk convection/diffusion is reduced. As a result, C_s can be significantly less than the far-downstream value C_o. This is clearly evident in Fig. 8, and demonstrates the importance of accurately calculating the bulk concentration field. The significance of

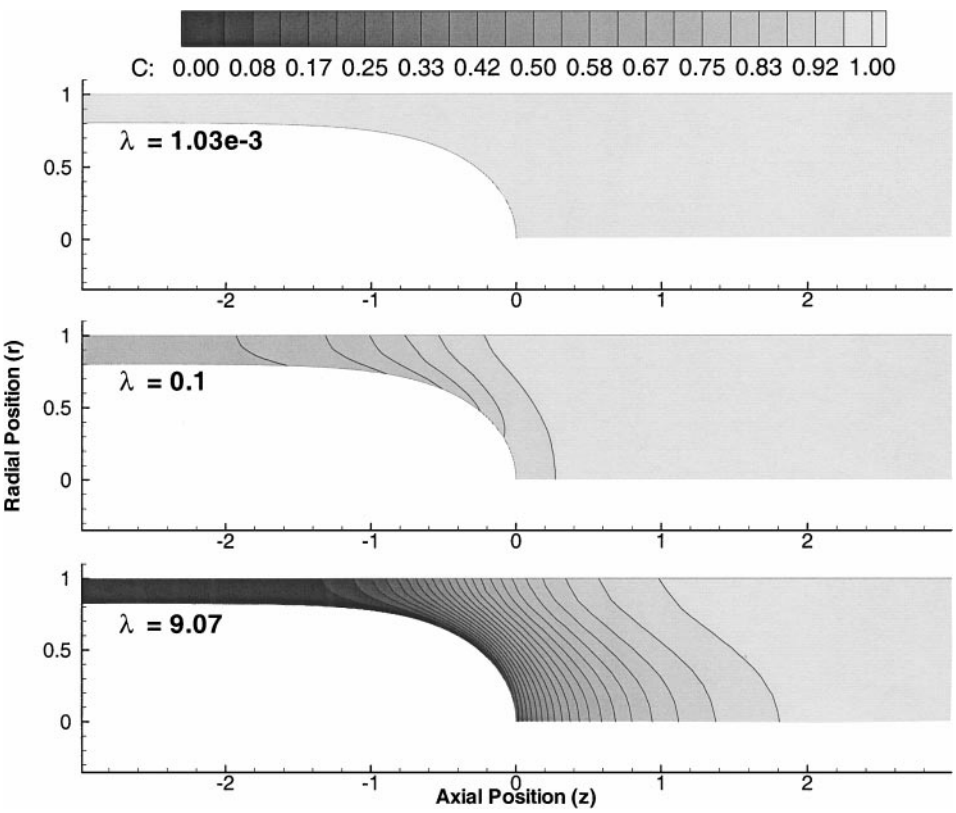

FIG. 8. Bulk concentration field surrounding the semi-infinite bubble for $\lambda = 1.03\text{e-}3, 0.1, 9.07$ and constant $\tilde{\Gamma}_{eq}$ by concurrently varying $St_a = \lambda St_d \tilde{\Gamma}_{eq}/(1 - \tilde{\Gamma}_{eq})$ ($Ca = 0.15$, $El = 0.5$, $St_d = 5$, $Pe = 10$, $Pe_s = 10^3$).

this transport behavior is further illustrated by the system's mechanical response as shown below.

4.4. *System Variables*

To identify the mechanical affect of bulk transport limitations that occur under low C_0 conditions, Fig. 9 demonstrates the variation of the dimensionless (a) bubble tip pressure drop, Π_{tip}; (b) tip curvature, κ_{tip}; (c) finger width, β_f; and (d) tip surface tension, γ_{tip}, as a function of λ for a constant $\tilde{\Gamma}_{eq}$.

Although κ_{tip}, β_f, and γ_{tip} are calculated as part of the iteration solution, to calculate Π_{tip} we follow the technique presented by Martinez and Udell [16]. The normal stress component at the interface following (3.6), can be expressed in terms of the normal velocity at the interface, u_n,

$$\hat{\boldsymbol{n}} \cdot (\sigma_{fluid} \cdot \hat{\boldsymbol{n}}) = -\prod_{fluid} + 2Ca\frac{\partial u_n}{\partial n} = \gamma\kappa. \tag{4.4}$$

Using continuity in an axisymmetric *n-s* coordinate system as $r \to 0$, (4.4) becomes

$$\prod_{tip} = -\prod_{fluid} = \gamma_{tip}\kappa_{tip} + 4Ca\frac{\partial u_s}{\partial s}, \tag{4.5}$$

where Π_{fluid} is the fluid pressure at the tip, $\Pi_{tip} = \Pi_{air} - \Pi_{fluid}$, and $\Pi_{air} = 0$ is the

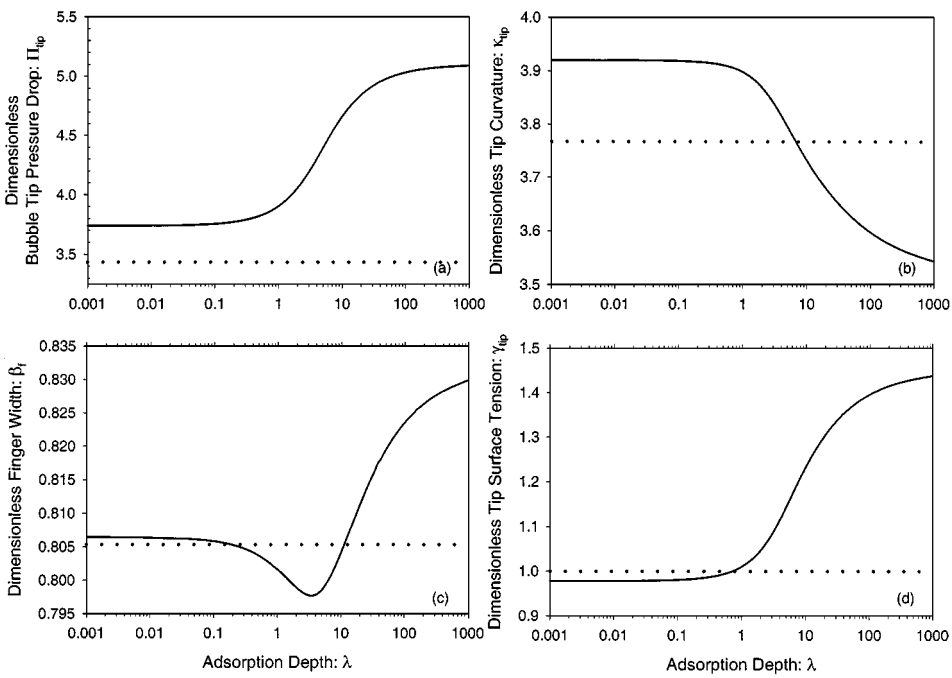

FIG. 9. Variation of the dimensionless (a) bubble tip pressure, (b) tip curvature, (c) finger width, and (d) tip surface tension as a function of λ for constant $\tilde{\Gamma}_{eq}$ by concurrently varying $St_a = \lambda St_d \tilde{\Gamma}_{eq}/(1 - \tilde{\Gamma}_{eq})$($Ca = 0.15$, $El = 0.5$, $\text{St}_d = 5$, $\text{Pe} = 10$, $Pe_s = 10^3$). Dotted horizontal lines indicate equilibrium values associated with $\lambda \to 0$ and $St_a \to \infty$.

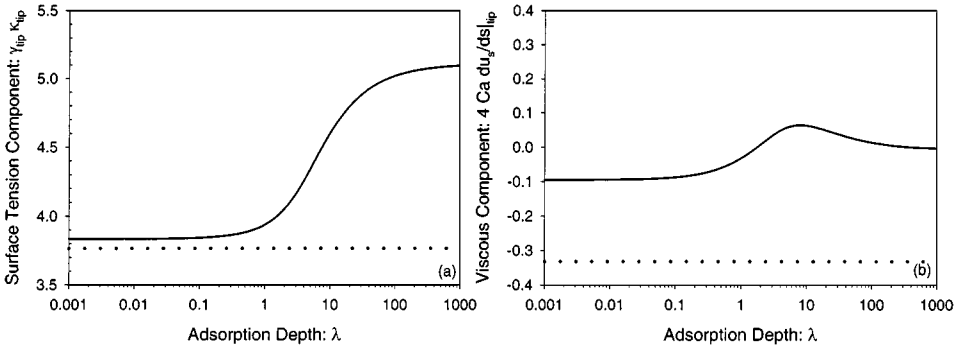

FIG. 10. Variation of (a) surface tension and (b) viscous components of Π_{tip} as a function of λ for constant $\tilde{\Gamma}_{eq}$ by concurrently varying $St_a = \lambda St_d \tilde{\Gamma}_{eq}/(1-\tilde{\Gamma}_{eq})$($Ca = 0.15$, $El = 0.5$, $St_d = 5$, $Pe = 10$, $Pe_s = 10^3$). Dotted horizontal lines indicate equilibrium values associated with $\lambda \to 0$ and $St_a \to \infty$.

reference pressure. Therefore, Π_{tip} has a surface tension component ($\gamma_{tip}\kappa_{tip}$) and a viscous component ($4Ca\ du_s/ds$), which are explored below.

As λ increases, Fig. 9a demonstrates that Π_{tip} increases monotonically. This increase in Π_{tip} is caused by the dramatic increase in γ_{tip} away from γ_{eq} (Fig. 9d) and thus an increase in the surface tension component (Fig. 10a). Note that although κ_{tip} decreases with increasing λ (Fig. 9b), the dramatic increase in γ_{tip} governs the monotonic increase in the surface tension component. Although the viscous component exhibits a slightly nonmonotonic behavior (Fig. 10b), the magnitude is significantly less than the surface tension component. Note that the dotted horizontal lines in Figs. 9 and 10 indicate the equilibrium values that would be observed if both bulk and adsorptive transport processes are rapid such that $\gamma = \gamma_{eq}$ uniformly. As $\lambda \to 0$, the bulk transport barrier is eliminated ($C_s = 1$) as shown in Fig. 8. However, the system remains adsorption-limited as $\lambda \to 0$ because of the fixed effective adsorption rate ($St_\lambda = 10$). As a result, the system variables do not approach the equilibrium values even at low λ.

To better explain the increase in the surface tension component of Π_{tip}, we consider the concentration and surface tension profiles. Figure 11 demonstrates the variation in the dimensionless (a) surface velocity, u_s; (b) surface concentration, Γ; (c) surface tension, γ; and (d) subsurface concentration, C_s, as a function of interfacial position for $\lambda = 1.03\text{e-}3$, 0.99, 9.70. As shown in Fig. 8, the bulk transport limitations result in a decrease in C_s with increasing λ (Fig. 11d). This decrease in C_s results in a decrease in Γ (Fig. 11b) and a concurrent increase in γ (Fig. 11c). The increase in γ_{tip} elevates the surface tension component which is responsible for the large Π_{tip} values observed at large λ. Therefore, the current model demonstrates that the quantity of surfactant transported to the interface can be significantly limited under low bulk concentration conditions.

Although, Γ, γ, and C_s are uniform in the thin film region (s > 4), surface convection near the bubble tip (s = 0) will generate a variation in these surface variables. The variation in γ shown in Fig. 11c will generate a Marangoni stress (τ_M) which is directed from regions of low γ to regions of high γ. This Marangoni stress, which rigidifies the interface, will alter the surface velocity profile, u_s (Fig. 11a). Specifically, at low λ, τ_M is small and u_s near the tip exhibits negative values. However, at larger λ, τ_M opposes the basic flow field and results in positive u_s near the tip. Thus, Marangoni stresses, which increase with λ, reduce or eliminate retrograde surface velocities near the tip.

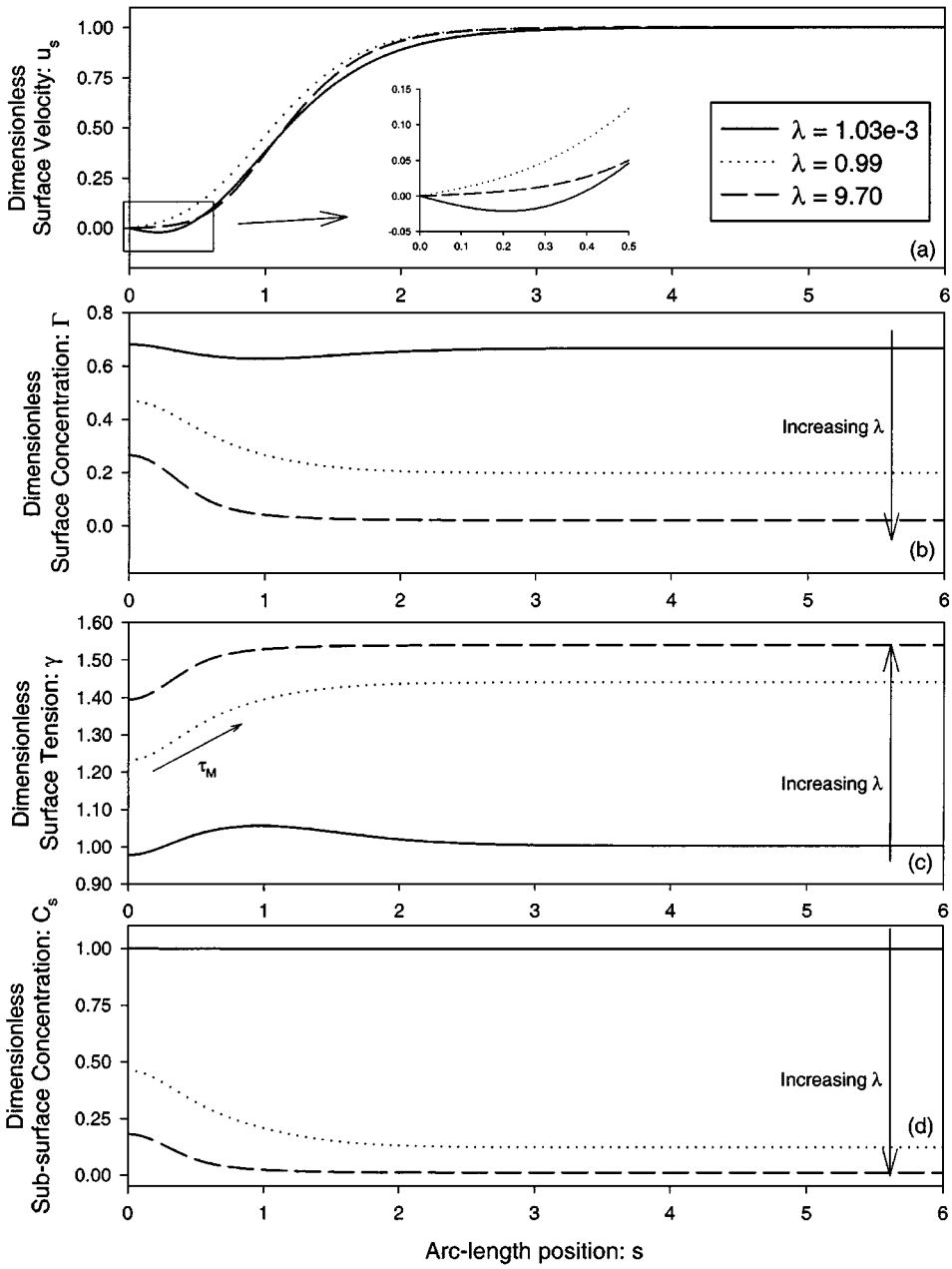

FIG. 11. Variation in the dimensionless (a) surface velocity, (b) surface concentration, (c) surface tension, and (d) subsurface concentration along the interface for $\lambda = 1.03\text{e-}3, 0.99, 9.70$ and constant $\tilde{\Gamma}_{eq}$ by concurrently varying $St_a = \lambda St_d \tilde{\Gamma}_{eq}/(1 - \tilde{\Gamma}_{eq})(Ca = 0.15, El = 0.5, St_d = 5, Pe = 10, Pe_s = 10^3)$.

The surface tension profile in Fig. 11c can also be used to explain the nonmonotonic behavior of β_f demonstrated in Fig. 9c. The magnitude of β_f is determined the magnitude of two forces, τ_M and the thin film surface tension (γ_{film}). As λ initially increases, the magnitude of τ_M near the bubble tip, which is directed toward the thin film, increases. As a result, fluid is driven into the thin film causing the film to thicken (reduction of β_f).

However, at large λ the stresses that tend to cause film thinning, namely a large γ_{film}, begin to dominate the Marangoni effect. Therefore, large γ_{film} values are responsible for the film thinning (increase in β_f) that is observed at large λ (Fig. 9c).

The behavior of this system as C_o is reduced (λ increased), indicates the importance of transport limitations on the mechanical behavior of the system. Clearly, if the bulk transport behavior is neglected, transport limitations will not be adequately modeled for low concentrations.

5. CONCLUSIONS

In this paper, we have demonstrated that the bulk convective/diffusive transport of surfactant in a free-surface flow system can be accurately and efficiently simulated with the dual-reciprocity boundary element method. Although DRBEM requires internal nodes, it is a grid-free method and therefore has advantages over the more traditional finite-element and finite-difference methods. Specifically, as the domain is modified to satisfy the free-surface boundary conditions, FEM and FDM would require an accurate re-meshing technique for the entire domain which can be computationally expensive. In contrast, the position of each internal node in DRBEM does not have to be structurally related to the position of neighboring nodes. Therefore, the expensive re-meshing step is not required and internal nodes can be placed in an unstructured fashion which results in increased computational efficiency.

Our motivation for this study was the development of an understanding of surfactant transport dynamics during respiratory distress syndrome (RDS) of premature infants, where it is well known that the primary pathology is due to a low bulk surfactant concentration. In this physiologically significant case, the true physicochemical dynamics cannot be adequately understood without accounting for bulk transport processes. A limitation of the current computational method is that convergence becomes increasingly difficult as Ca decreases to values below 10^{-2}. However, Yap [30] predicted that for several adult and infant physiological conditions $0.01 < Ca < 10$. Since the current computational model is capable of accurately simulating this range, the current theoretical analysis is applicable to the *in-vivo* system.

Another limitation of this computational approach relates to the resolution of concentration boundary layers. These boundary layers are likely to be small at large Pe. We have demonstrated that resolution of the concentration field is accurate for $Pe = 10$, however accurate calculations beyond this value may become increasingly difficult. Nevertheless, the results for $Pe = \mathrm{O}(10)$ do qualitatively demonstrate behavior that will exist when convection dominates diffusion, and thus may be useful in understanding systems where Pe is even larger.

The current model extends beyond previous models of surfactant transport in systems that may relate to airway reopening. First, the adsorption kinetics and equation of state are modeled using the nonlinear Langmuir adsorption model. Most previous studies [24, 28, 31] used a linear relationship between the surfactant concentration and the local surface tension. However, linear models are only valid for small departures from equilibrium, and experiments have demonstrated that pulmonary surfactant analogues exhibit nonlinear equations of state [8, 14]. Therefore, the inclusion of nonlinear Langmuir dynamics is essential to the accurate simulation of this physiological system.

In addition, the methods developed herein compute the complete steady-state bulk convection–diffusion equation without approximation. Previous investigators [28, 31] have

investigated bulk equilibrium systems in which the bulk concentration is assumed to be uniform. This assumption is only valid if the bulk concentration is very large. Under these conditions, C_o is large ($\lambda \ll 1$), and the solution to (3.17) is simply $C(r, z) = 1$.

Our studies indicate that the transport limitations that can occur at low surfactant concentrations can lead to large reopening pressures which may damage the airway wall and thus contribute to the pathology or positive feedback cycle that can result in infant death. Therefore, modeling RDS conditions requires a solution of the full convection–diffusion problem as performed in this study. In the future, we will use this method to determine the conditions under which bulk transport limitations and surfactant physicochemical properties can influence the clinically relevant reopening pressures by limiting the quantity of surfactant that can be transported to the interface.

APPENDIX

As discussed by Sarler [26] the axisymmetric interpolating function, ϕ_j and f_j, can be obtained by integrating the appropriate three-dimensional versions. For the following three-dimensional definition of ϕ_j,

$$\phi_j^{3D}(x, y, z) = 1 + \rho_j(x, y, z) = 1 + \sqrt{(x - x_j)^2 + (y - y_j)^2 + (z - z_j)^2}, \qquad \text{(I.1)}$$

the three-dimensional f_j is

$$f_j^{3D} = \rho_j^2/6 + \rho_j^3/12. \qquad \text{(I.2)}$$

In an axisymmetric coordinate system, $x = r\cos\theta$, $y = r\sin\theta$, $x_j = r_j\cos\theta_j$, and $y_j = r_j\sin\theta_j$. Setting $\theta = 0$ as the reference point, the following integration yields the axisymmetric form of ϕ_j:

$$\phi_j(r, z) = \frac{1}{2\pi}\int_0^{2\pi} \phi_j^{3D} d\theta = 1 + \frac{2}{\pi} C_p E(m_p)$$
$$\text{where } C_p = \sqrt{(r + r_j)^2 + (z - z_j)^2} \quad \text{and} \quad m_p = \frac{2\sqrt{r r_j}}{C_p}. \qquad \text{(I.3)}$$

Here, $E(m_p)$ is the complete elliptic integral of the second kind as defined by Abramowitz and Stegun [1]. In a similar fashion, we can determine the axisymmetric from of f_{ij},

$$f_j(r, z) = \frac{1}{2\pi}\int_0^{2\pi} f_j^{3d} d\theta = \frac{r^2 + r_j^2 + (z - z_j)^2}{6} + \frac{C_p^3 \sigma_p(m_p)}{18\pi}$$
$$\text{where } \sigma_p(m_p) = 2\left(2 - m_p^2\right)E(m_p) - \left(1 - m_p^2\right)K(m_p). \qquad \text{(I.4)}$$

Here, K(m_p) is the complete elliptic integral of the 1st kind as defined by Abramowitz and Stegun [1]. In addition to these expressions, the expression for $df_j/d\hat{\boldsymbol{n}}$ can be obtained

from (I.4),

$$\frac{df_j}{d\hat{\boldsymbol{n}}} = \frac{df_j}{dr}n_r + \frac{df_j}{dz}n_z$$

$$\frac{df_j}{dr} = \frac{r}{3} + \frac{C_p}{12\pi r}\left[\left\{C_p^2\left(1-2m_p^2\right) + 6r\left(r+r_j\right)\right\}E\left(m_p\right) - C_p^2\left(1-m_p^2\right)K\left(m_p\right)\right] \quad \text{(I.5)}$$

$$\frac{df_j}{dz} = \frac{(z-z_j)^2}{3} + \frac{C(z-z_j)E(m_p)}{2\pi}.$$

Finally, because of the singular nature of the elliptic integrals as well as the functions themselves, we must consider the following limits. First, if $r = r_j$ and $z = z_j$ then

$$\begin{aligned} \phi_j &= 1 + \frac{2C_p}{\pi} \\ f_j &= \frac{r^2}{3} + \frac{C_p^3}{9\pi} \\ \frac{df_j}{d\hat{\boldsymbol{n}}} &= \left(\frac{r}{3} + \frac{2C_p r}{3\pi}\right)n_r. \end{aligned} \quad \text{(I.6)}$$

Second, if $r = 0$ or $r_j = 0$ then

$$\begin{aligned} \phi_j &= 1 + C_p \\ f_j &= \frac{r^2 + r_j^2 + (z-z_j)^2}{6} + \frac{C_p^3}{12} \\ \frac{df_j}{d\hat{\boldsymbol{n}}} &= \left(\frac{r}{3} + \frac{C_p(r+r_j)}{4}\right)n_r + \left(\frac{(z-z_j)}{3} + \frac{C_p(z-z_j)}{4}\right)n_z. \end{aligned} \quad \text{(I.7)}$$

ACKNOWLEDGMENTS

This research was funded by National Science Foundation Grants BES-9978605 and DMF-9709754, the National Institutes of Health Grant R29-HL51334, and a Special Opportunity Award from the Whitaker Foundation.

REFERENCES

1. M. Abramowitz and C. A. Stegun, *Handbook of Mathematical Functions with Formulas, Graphs, and Mathematical Tables* (Dover, New York, 1972), 9th Printing.
2. J. D. Anderson, *Computational Fluid Dynamics: The Basics with Applications* (McGraw-Hill, New York, 1995).
3. A. A. Becker, *The Boundary Element Method in Engineering: A Complete Course* (McGraw-Hill, New York, 1992).
4. F. P. Bretherton, The motion of long bubbles in tubes, *J. Fluid Mech.* **10**, 166 (1961).
5. D. J. Coyle, C. W. Macosko, and L. E. Scriven, Film-splitting flows in forward roll coating, *J. Fluid Mech.* **171**, 183 (1986).
6. C. D. Eggleton, Y. P. Pawar, and K. J. Stebe, Insoluble surfactants on a drop in an extensional flow: a generalization of the stagnated surface limit to deforming interfaces, *J. Fluid Mech.* **385**, 79 (1999).
7. D. P. Gaver, III, D. Halpern, O. E. Jensen, and J. B. Grotberg, The steady motion of a semi-infinite bubble through a flexible-walled channel, *J. Fluid Mech.* **319**, 25 (1996).
8. S. N. Ghadiali and D. P. Gaver, III, An Investigation of Pulmonary Surfactant Physicochemical Behavior under Airway Reopening Conditions, *J. Appl. Physiol.* **88**, 493 (2000).

9. M. D. Giavedoni and F. A. Saita, The axisymmetric and plane cases of a gas phase steadily displacing a Newtonian liquid—A simultaneous solution of the governing equations, *Phys. Fluids* **9**(8), 2420 (1997).
10. G. M. Ginley and G. M. Radke, Influence of soluble surfactants on the flow of long bubbles through a cylindrical capillary, *ACS Symposium Series* **396**, 480 (1988).
11. D. Halpern and D. P. Gaver, III, Boundary element analysis of the time-dependent motion of a semi-infinite bubble in a channel, *J. Comput. Phys.* **115**, 366 (1994).
12. R. A. Johnson and A. Borhan, Effect of Insoluble Surfactants on the Pressure-Driven Motion of a Drop in a Tube in the Limit of High Surface Coverage, *J. Colloid Interface Sci*. **218**, 184 (1999).
13. O. A. Ladyzhenskaya, *The Mathematical Theory of Viscous Incompressible Flow* (Gordon and Breach, New York, 1963).
14. M. M. Lipp, K. Y. C. Lee, J. A. Zasadzinski, and A. J. Waring, Phase and morphology changes in lipid monolayers induced by SP-B protein and its amino-terminal peptide. *Science* **273**(5279), 1196 (1996).
15. M. J. Martinez and K. S. Udell, Axisymmetric creeping motion of drops through circular tubes. *J. Fluid Mech*. **210**, 565 (1990).
16. M. J. Martinez and K. S. Udell, Boundary integral analysis of the creeping flow of long bubbles in capillaries. *J. Appl. Mech.* **56**, 211 (1989).
17. W. J. Milliken, H. A. Stone, and L. G. Leal, The effect of surfactant on the transient motion of Newtonian drops, *Phys. Fluids A* **5**(1), 69 (1993).
18. D. Myers, *Surfaces, Interfaces, and Colloids* (VCH, New York, 1991).
19. C. W. Park and G. W. Homsy, Two-phase displacement in Hele-Shaw cells, *J. Fluid Mech*. **139**, 291 (1984).
20. P. W. Partridge, C. A. Brebbia, and L. C. Wrobel, *The Dual Reciprocity Boundary Element Method* (Computational Mechanics, Southampton, 1992).
21. W. H. Press, B. P. Flannery, S. A. Teukolsky, and W. T. Vetterling, *Numerical Recipes: The Art of Scientific Computing* (Cambridge Univ. Press, Cambridge, UK, 1989).
22. J. Prothero and A. C. Burton, The physics of blood flow in capillaries, *J. Biophys*. **2**, 525 (1961).
23. P. A. Ramachandran, *Boundary Element Methods in Transport Phenomena* (Computational Mechanics, Southampton, 1994).
24. J. Ratulowski and H.-C. Chang, Marangoni effects of trace impurities on the motion of long gas bubbles in capillaries, *J. Fluid Mech*. **210**, 303 (1990).
25. D. A. Reinelt and P. G. Saffman, The penetration of a finger into a viscous fluid in a channel and tube, *SIAM J. Sci. Stat. Comput.* **6**(3), 542 (1985).
26. B. Sarler. Axisymmetric augmented thin plate splines. *Eng. Anal. Boundary Elem*. **21**, 81 (1998).
27. E. I. Shen and K. S. Udell, A Finite Element study of low Reynolds number two-phase flow in cylindrical tubes, *J. Appl. Mech.* **52**, 253 (1985).
28. K. J. Stebe and D. Barthès-Biesel, Marangoni effects of adsorption-desorption controlled surfactants on the leading end of an infinitely long bubble in a capillary, *J. Fluid Mech*. **286**, 25 (1995).
29. H. A. Stone and L. G. Leal, The effects of surfactants on drop deformation and breakup, *J. Fluid Mech*. **220**, 161 (1990).
30. D. Y. K. Yap, *A Computational Study of the Physicochemical Influence of Surfactant Under Bulk-Equilibrium Conditions on Pulmonary Airway Reopening*, Ph.D. Thesis (Department of Biomedical Engineering, Tulane University, New Orleans, LA, 1997).
31. D. Y. K. Yap and D. P. Gaver, III, The influence of surfactant on two-phase flow in a flexible-walled channel under bulk equilibrium conditions, *Phys. Fluids* **10**(8), 1846 (1998).